PHYSICAL REVIEW B **94**, 134413 (2016)

Employing soft x-ray resonant magnetic scattering to study domain sizes and anisotropy in Co/Pd multilayers

Kai Bagschik,[1,2,*] Robert Frömter,[1,2] Judith Bach,[1] Björn Beyersdorff,[1] Leonard Müller,[3] Stefan Schleitzer,[3]
Magnus Hårdensson Berntsen,[3,4] Christian Weier,[5] Roman Adam,[5] Jens Viefhaus,[6] Claus Michael Schneider,[5]
Gerhard Grübel,[2,3] and Hans Peter Oepen[1,2]
[1]*Institut für Nanostruktur- und Festkörperphysik, Jungiusstraße 11, 20355 Hamburg, Germany*
[2]*The Hamburg Centre for Ultrafast Imaging, Luruper Chaussee 149, 22761 Hamburg, Germany*
[3]*Deutsches Elektronen-Synchrotron (DESY), FS-CXS, Notkestraße 85, 22607 Hamburg, Germany*
[4]*KTH Royal Institute of Technology, ICT Materials Physics, Electrum 229, 164 40 Kista, Sweden*
[5]*Peter Grünberg Institut, PGI-6 and JARA-FIT, Forschungszentrum Jülich, 52425 Jülich, Germany*
[6]*Deutsches Elektronen-Synchrotron (DESY), FS-PE, Notkestraße 85, 22607 Hamburg, Germany*

(Received 18 December 2015; revised manuscript received 12 August 2016; published 12 October 2016)

It is demonstrated that the magnetic diffraction pattern of the isotropic disordered maze pattern is well described utilizing a gamma distribution of domain sizes in a one-dimensional model. From the analysis, the mean domain size and the shape parameter of the distribution are obtained. The model reveals an average domain size that is significantly different from the value that is determined from the peak position of the structure factor in reciprocal space. As a proof of principle, a wedge-shaped $(\mathrm{Co}_{t\text{Å}}/\mathrm{Pd}_{10\text{Å}})_8$ multilayer film, that covers the thickness range of the spin-reorientation transition, has been used. By means of soft x-ray resonant magnetic scattering (XRMS) and imaging techniques the thickness-driven evolution of the magnetic properties of the cobalt layers is explored. It is shown that minute changes of the domain pattern concerning domain size and geometry can be investigated and analyzed due to the high sensitivity and lateral resolution of the XRMS technique. The latter allows for the determination of the magnetic anisotropies of the cobalt layers within a thickness range of a few angstroms.

DOI: 10.1103/PhysRevB.94.134413

I. INTRODUCTION

Challenges in modern research on magnetism are directly related to the realization of ever smaller and faster magnetic storage devices. Magnetization reversal processes at ultrafast time and nanometer length scales pave the way to higher storage densities and higher read/write speeds. Experimental tools for investigating the magnetization with high spatial resolution and element specificity are required to develop such devices and their complex chemical composition. X-ray-based techniques allow for studying magnetic domain structure by employing the circular dichroism at the absorption edge of a selected magnetic element. Real-space x-ray techniques are full-field (MTXM) and scanning x-ray microscopy (STXM) [1–3], while Fourier-space techniques are Fourier transform holography (FTH) [4–6], x-ray holographic microscopy (XHM) [7], x-ray ptychography [8,9] and x-ray resonant magnetic scattering (XRMS) [10–15]. XRMS is commonly used to obtain ensemble-averaged information from the multidomain state that naturally occurs in systems with out-of-plane easy axis of magnetization. Characteristic average properties, such as average domain size and lateral correlation length, can be extracted. Ultrafast dynamic processes in magnetic materials are often studied utilizing XRMS in pump-probe experiments because of the high photon efficiency combined with the high photon flux available at free-electron laser sources allowing for single-shot measurements [16,17]. However, the interpretation of the magnetic diffraction patterns and their correlation to the real-space domain structure is a big issue [18]. Magnetic models are required for the meaningful analysis of diffraction patterns from diverse domain structures. Models exist describing the diffraction pattern of well-aligned stripe domain patterns based on a one-dimensional periodic lattice [19]. Hellwig *et al.* [20] have presented an extended ansatz to analyze scattering patterns of moderately disordered stripe domain structures by implementing Gaussian fluctuations in the domain size. The interpretation of diffraction patterns from highly disordered two-dimensional maze domain patterns, where the domain walls are mostly curved and almost no straight sections occur, is still under debate. The scattering pattern of such a two-dimensional simulated domain structure has been analyzed in [18], where a peak shift towards smaller momentum transfer Q has been found upon domain-wall broadening.

In this paper, we report on XRMS experiments to investigate highly disordered magnetic maze patterns utilizing a wedge-shaped multilayer sample. As a model system a wedge-grown Co/Pd multilayer film is used that shows a thickness-driven spin-reorientation transition (SRT) from out-of-plane to in-plane orientation of magnetization. In the thickness range where the effective first-order anisotropy constant becomes small the domain size decreases upon thickness increase and eventually the magnetization starts canting into the film plane. The investigation of the domain pattern in the latter thickness range is a formidable task as the orientation of magnetization is highly susceptible to magnetic fields [21,22]. Due to the latter film property, techniques that come along with local magnetic fields, such as scanning probe techniques [23,24], cannot be used to study the magnetic domain size in the range of zero crossing of the effective first-order anisotropy constant. For the investigation of the latter magnetic system all optical methods, e.g., small-angle scattering, are most advantageous as magnetic fields are circumvented.

---

[*] Corresponding author: kbagschi@physnet.uni-hamburg.de

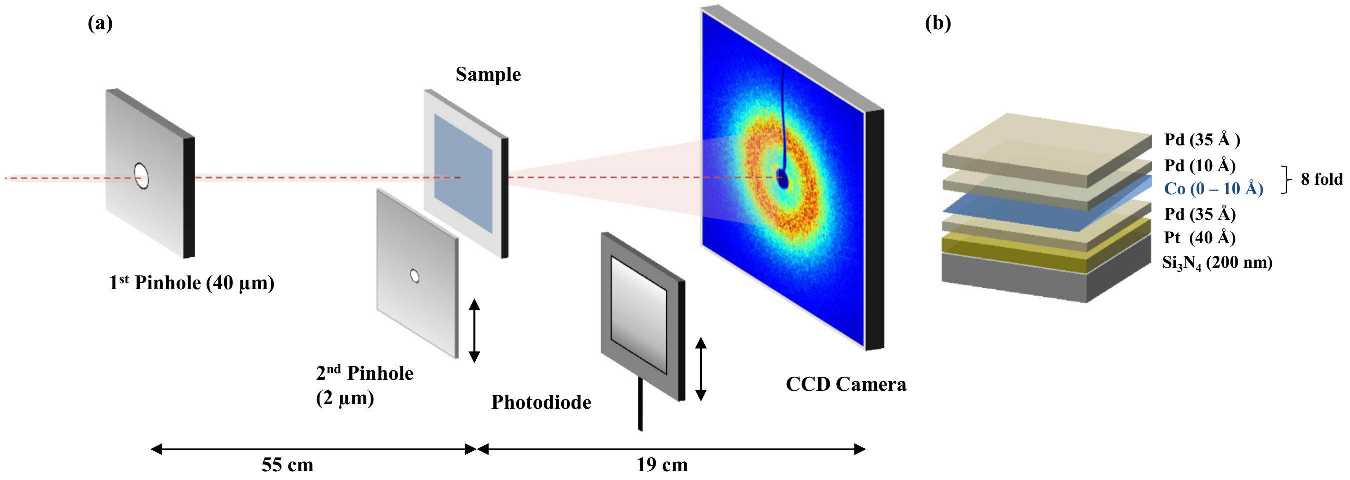

FIG. 1. (a) Layout of the XRMS experiment at the P04 beamline of Petra III. The beam coming from the left passes through a pinhole with a diameter of 40 μm, and is scattered at the sample. The scattering pattern is recorded by a CCD camera. The direct beam is blocked by a beam stop. Optionally a second pinhole and a photodiode can be placed before and behind the sample to record absorption. (b) Sketch of the Co/Pd sample system.

Static structure factors are extracted as a function of cobalt thickness. For the interpretation of the changing structure factors we present a model describing the highly disordered maze domain structure. The model is based on a one-dimensional pattern with gamma-distributed domain sizes to imply the significant domain size variations. It is described by the mean domain size, the domain-wall width, and the shape parameter of the distribution that is characteristic for a certain pattern. A very good agreement of simulations and experiment is obtained.

In the last chapter, a cross-check is performed to test the model by means of extracting the magnetic properties from the domain size. In a first step, the effective first-order magnetic anisotropy constant is determined from the domain sizes, which yields the thickness dependence of the anisotropy. The result is an inverse-thickness dependence of the anisotropy which is expected for a thickness-driven spin reorientation. The results fit very well with data of previous investigations [25–28]. It has to be emphasized that the resolution of the small-angle scattering allows for the determination of anisotropies within a thickness range of only a few angstroms in the immediate vicinity of the SRT.

II. EXPERIMENT

The wedge-shaped multilayer film consists of an eightfold Co/Pd bilayer $(\mathrm{Co}_{t\text{Å}}/\mathrm{Pd}_{10\text{Å}})_8$ where the thickness of each Co single layer is varied from $t_{\mathrm{Co,single}} = 0$ to 10 Å, and the Pd layer thickness is kept constant. The multilayer is fabricated using dc magnetron sputtering at room temperature utilizing the penumbra of a shadow mask. The film system is fabricated on a 200-nm-thick $\mathrm{Si_3N_4}$ membrane of $1500 \times 1500\,\mu\mathrm{m}^2$ size. First, seed layers of 4-nm Pt (plasma-based ion-beam sputtering) and 3.5-nm Pd (dc magnetron sputtered) are grown. On the seed layer, the Co/Pd multilayer stack is deposited (dc magnetron sputtered) and capped by a 3.5-nm Pd layer [29–31] [Fig. 1(b)]. In the following $t_{\mathrm{Co,total}}$ is the total Co multilayer thickness, which is the sum of thicknesses of all layers of the multilayer, and $t_{\mathrm{Co,single}}$ is the Co single-layer thickness.

Figure 1(a) displays a sketch of the XRMS setup. The beam coming from the left first passes through a pinhole with a diameter of 40 μm which selects the coherent part of the beam and defines the illuminated area on the sample. The sample can be positioned in the plane perpendicular to the beam with nanometer resolution utilizing a piezoelectrically driven stage. The scattered x rays are detected by a Peltier-cooled 16 Mpx charge-coupled device (CCD) camera with a pixel size of $15 \times 15\,\mu\mathrm{m}^2$. The camera is protected from the high-intensity zero-order beam by a central beam stop of 1 mm diameter.

The measurements were performed at the P04 beamline of the storage ring PETRA III which is equipped with an APPLE II undulator delivering circularly polarized x rays with energies ranging from 250 to 3000 eV [32]. Focusing mirrors provide 10 μm beam size in vertical and 100 μm beam size in horizontal directions at focal lengths of 2.5 and 16.9 m (the latter well behind our setup), respectively. At the first pinhole the beam is convergent in the vertical direction and collimated in the horizontal direction. The sample is placed 18 cm behind the vertical focus. At the sample position, the beam size is $\approx 30\,\mu\mathrm{m} \times 45\,\mu\mathrm{m}$ FWHM utilizing a 40-μm pinhole. To measure the coherence of the beam we performed a Young´s double-pinhole experiment. Using the 40-μm illumination pinhole and a monochromator exit slit of 200 μm, a transverse coherence length of more than 15 μm in both horizontal and vertical directions was obtained [33].

III. SAMPLE CHARACTERIZATION

The calibration of the total Co thickness is performed *in situ*. The sample is scanned across the beam and the transmitted intensities are measured using the photodiode. An additional pinhole of 2 μm diameter, placed directly in front of the sample, defines the spatial resolution of this measurement. Absorption profiles along and perpendicular to the wedge are

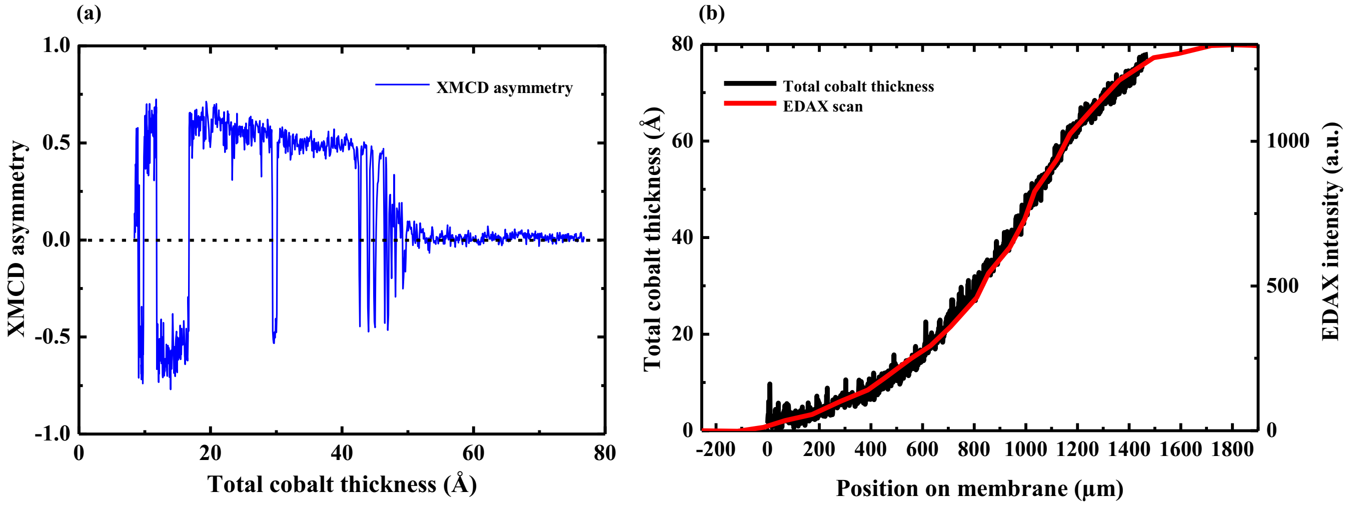

FIG. 2. (a) The XMCD asymmetry along the wedge at the Co L_3 edge (778 eV) calculated from the transmitted intensities with left- and right- circular polarization. (b) Co thickness calculated from absorption profiles with opposite helicities at 778 eV (black lines) and calibrated with an EDAX profile along the wedge (red line).

taken at $h\nu = 778$ eV (Co L_3 edge) with left- and right-circular polarization. Absorption profiles taken perpendicularly to the wedge show constant intensity which means that the Co thickness is constant. The Co thickness profile along the wedge is determined from the average of the transmitted intensities at $h\nu = 778$ eV for both helicities $I^{778}_{\mathrm{avg}} = (I^{778}_{+} + I^{778}_{-})/2$. For comparison and calibration purposes, line profiles were taken utilizing energy-dispersive x-ray spectroscopy (EDX) in a scanning electron microscope [Fig. 2(b), red solid line]. The EDX signal of Co depends linearly on Co thickness within the studied thickness range, which was checked by Monte Carlo simulations. Scaling with respect to the known thickness of 80 Å at the top of the wedge, the EDX profile can be used to calibrate the transmitted intensities. We obtain a penetration length of 41 nm describing the transmitted intensity via the Beer-Lambert law [Fig. 2(b), black solid line]. Due to the limited size of the Si_3N_4 membrane a total Co thickness from $t_{\mathrm{Co,total}} = 1$ to 76 Å is accessible in the x-ray investigation.

Figure 2(a) shows the magnetic asymmetry $(\mu^{778}_{+} - \mu^{778}_{-})/(\mu^{778}_{+} + \mu^{778}_{-})$ (blue line), with $\mu^{778}_{+/-} = -\ln(I^{778}_{+/-}/I_0)(1/t_{\mathrm{Co,total}})$, caused by the different orientations of magnetization. The asymmetry reveals changes in the magnetization profile with a spatial resolution of about 1 μm (resulting from the convolution of a 2-μm circular aperture with a step function). The maximum of the asymmetry is 0.62 at the onset of ferromagnetism and it decreases gradually towards 0.50. The dichroic contrast vanishes above 51 Å total Co thickness, where the domains become too small to be laterally resolved with the 2-μm pinhole. The change of the magnetic circular dichroism (XMCD) asymmetry with decreasing Co thickness is presumably originating from an enhanced orbital angular momentum m_{orb} which has been found in Co/Pt multilayers below $t_{\mathrm{Co,single}} \approx 8$ Å [34].

IV. SOFT X-RAY RESONANT MAGNETIC SCATTERING

An overview of the magnetic domain pattern is obtained by locally measuring the absorption at $h\nu = 778$ eV utilizing the same experimental setup as above. The sample is scanned across the fixed pinhole in two directions perpendicular to the beam. The latter procedure is analogous to scanning transmission x-ray microscopy (STXM). Figure 3(a) displays the domain pattern as a function of the Co thickness. The STXM image can be used to determine the average domain sizes along the wedge. Using stereological methods [35,36], domain sizes from $\sim 4\,\mu$m down to $\sim 2.4\,\mu$m are found in a total Co thickness range of $t_{\mathrm{Co,total}} = 46 \pm 0.4$ Å to 49 ± 0.4 Å. Smaller domains cannot be resolved due to the limited spatial resolution ($\sim 1\,\mu$m). In the range of the smallest domain sizes, a loss of contrast both in the STXM image [Fig. 3(a)] and in the line scan of the magnetic asymmetry [Fig. 2(a)] can be seen.

In order to investigate domains with sizes in the nanometer range, we performed XRMS at $h\nu = 778$ eV. The spatial resolution of XRMS is limited by the wavelength ($\lambda_{778} = 1.59$ nm) and the detectable maximum momentum transfer Q. In general, however, signal-to-noise limitations are relevant due to the dynamic range of the detector and the photon statistics as the intensity drops strongly towards higher Q. As the perpendicularly magnetized multilayer displays a mazelike domain configuration, the scattered x rays are expected to show an isotropic donutlike diffraction pattern [Fig. 3(b)] with a characteristic radius of maximum intensity $Q_{\max}$ correlated to the domain size. The static structure factor $S(Q) \propto I(Q) \propto |\int_n f_n e^{iQR}|^2$ as a function of momentum transfer Q is extracted from the CCD images by radially averaging the measured photon intensity along circles around the center of the diffraction pattern [Fig. 3(c)]. The resonant scattering amplitude $f_n = f_n^{\mathrm{charge}} + f_n^{\mathrm{magnetic}}$ contains a charge contribution and a magnetic scattering contribution, where the charge contribution corresponds to a nonresonant (classical Thomson scattering) as well as a resonant charge term. The charge contribution f_n^{charge} can be assumed to be constant and can be neglected for the multilayer, as correlations of charge inhomogeneities on the length scale of 100 nm do not exist in the sample under investigation (grain sizes $\leqslant 10$ nm [37,38]). The magnetic term f_n^{magnetic} comprises the magnetic

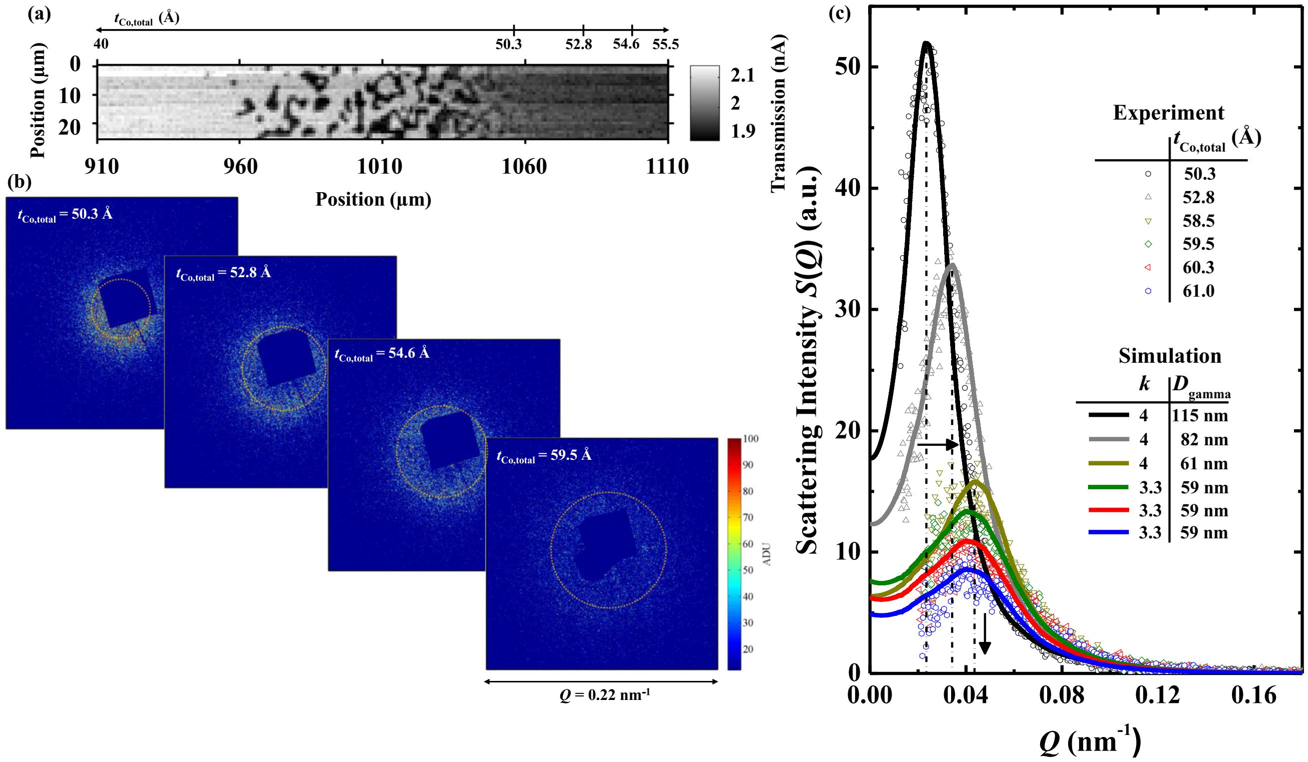

FIG. 3. (a) Scanning transmission x-ray microscopy (STXM) image at $h\nu = 778$ eV showing the domain size evolution with increasing Co thickness. (b) X-ray scattering patterns of magnetic domains. The rectangular structure in the center is used to mask out the superimposed projection image of the membrane window. Yellow dashed-line circles indicate the maximum of the structure factor for each Co thickness. (c) Intensity profiles extracted from the diffraction pattern via radial integration (colored symbols). We observe a shift of the peak position Q_{max} (black horizontal arrow), as well as a decrease of the scattering intensity and an increase of peak width. Above a total Co thickness of $t_{\mathrm{Critical}} = 58.5 \pm 0.4$ Å the peak positions stay constant in Q while the intensity continues to drop (black vertical arrow). The solid lines are simulated intensity profiles resulting from a FFT of a one-dimensional domain pattern with gamma-distributed domain sizes.

circular dichroism (XMCD) [13,39–41], which exhibits a linear dependency on the normal component of the magnetic moment m_z.

A series of magnetic diffraction patterns were recorded at different Co thicknesses [Fig. 3(b)] and used to extract the corresponding structure factors $S(Q)$ [Fig. 3(c)]. The intensity profiles reveal a shift of the peak positions Q_{max} towards larger Q values for increasing Co thickness within a total Co thickness range of $t_{\mathrm{Co,total}} = 50.3 \pm 0.4$ Å to 58.5 ± 0.4 Å [Fig. 3(c)]. Additionally, a variation of the intensity profiles in width and amplitude with increasing Q_{max} can be recognized. Above a total thickness of $t_{\mathrm{Critical}} = 58.5 \pm 0.4$ Å the peak positions remain at the same Q, while the intensity continues to drop.

To understand the evolution of the intensity profiles on Q_{max}, a model is required that comprises the spatially disordered mazelike domain pattern. For a well-aligned stripe pattern a model has already been published [20] in which spatial disorder is included by implementing additional cumulative Gaussian fluctuations of the domain size to explain the finite peak width of the structure factor. The maze pattern exhibits only a short-range correlation which is a striking difference to the long-range correlations of stripe domains [19,20]. Here, large variations of domain sizes have to be considered as indicated by a broad peak of the structure factor.

V. SCATTERING MODEL FOR THE MAZE PATTERN

The model describing the magnetic domains in maze patterns can be realized by micromagnetic simulation of a sufficiently large area which is needed to attain reasonable statistics after the Fourier transform. The simulation of large samples with high spatial resolution is not practical, due to limits of computing time. A second problem of the micromagnetic simulation is that special procedures are needed to extract the geometric parameters from the simulated two-dimensional domain pattern.

However, the donutlike diffraction pattern implies that on the average, the domain size and the width distribution are isotropic. The isotropy allows a one-dimensional description as it keeps all information contained in the scattering profile. From the mathematical point of view a two-dimensional domain pattern can be decomposed into a sum of stripe patterns with varying domain width and orientation [42]. Each stripe pattern corresponds in Fourier space to a fixed spatial frequency and its complex conjugate partner. Radial averaging in Fourier space projects all orientations onto one direction which leads to an averaged one-dimensional pattern representing all information of the domain widths of the two-dimensional domain pattern. Thus, to a good approximation a one-dimensional domain pattern can be used to describe

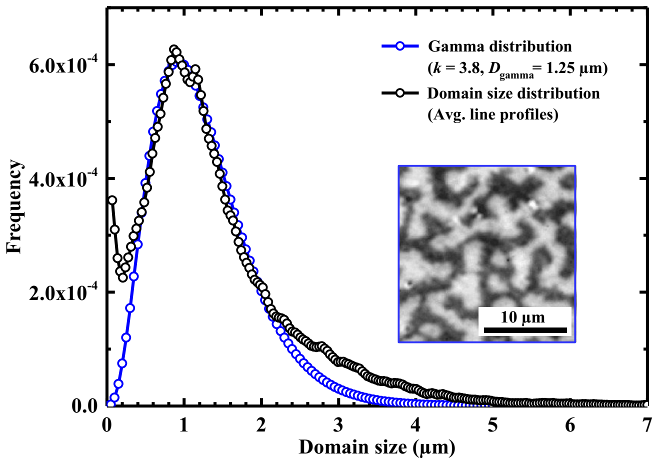

FIG. 4. Comparison of the domain size distribution of a maze pattern from a Nd-Fe-B sample extracted from line profiles (black circles) with the probability density function of a gamma distribution (blue circles) fitted to the data. The inset shows a part of a Kerr image from this sample. The domain size distribution and the Kerr image have been taken from Fig. 2 in Ref. [43] (Courtesy of Dr. Juliane Thielsch and Dr. Thomas G. Woodcock). A good agreement of both curves is apparent. The increasing frequencies at very small domain sizes occur from wavy domain walls specific to the system (see Ref. [43]). Only in the range between 2 and 3 times the mean domain size deviations are present.

a two-dimensional domain system when an isotropic two-dimensional diffraction pattern is obtained in the experiment.

Here, we propose as a refined model a one-dimensional domain pattern with gamma-distributed domain sizes to fit the experimentally observed structure factors. To justify such a model, we have compared a published domain size distribution of a maze pattern with a gamma distribution. Thielsch *et al.* [43] have analyzed a Kerr microscopy image of a Nd-Fe-B sample by taking line profiles along different directions and measuring the distances between domain walls. This analysis (reproduced in Fig. 4 from Fig. 2(b) in Ref. [43]) yields a strongly asymmetric distribution of domain sizes which is at variance with a symmetric Gaussian peak shape. The distribution falls off faster towards small domain sizes and extends wider towards large domains. Using the extracted domain size distribution and fitting with the probability density function of the gamma distribution, a good agreement of both curves is obtained. A mean domain size of 1.25 μm and a shape parameter of $k = 3.8$ result from the fit. One systematic deviation of the model is a small underestimation of the frequency for domain sizes in the range of 2 to 3 times the mean value. The total weight of this deviation is about 7%. A second difference is the increase of frequency at very small domain sizes. This is discussed in [43] as a consequence of wavy domain walls specific to this system, a feature we do not observe in our Co/Pd films. For this example it is clear that the domain size distribution of the two-dimensional maze pattern is fairly well described by a one-dimensional gamma distribution. A more complicated empirical distribution function might give a more exact agreement, but this requires an increased number of fit parameters and might thus be less meaningful.

The number of parameters to describe this distribution is two, just as for the case of a Gaussian description, so the complexity of the model is not increased. Hence a gamma-distributed domain size appears to be reasonable for modeling a more realistic domain pattern in the range of the spin reorientation.

A one-dimensional array of domains is created, with values +1 (–1), for up (down) magnetized domains. The size of the domains is generated numerically by gamma-distributed random numbers. The total length of the array is several millimeters with an element size of 0.1 nm. A subsequent fast Fourier transform (FFT) gives the structure factor $S(Q)$ as a function of momentum transfer Q for the given magnetic domain pattern. The probability density function of the gamma distribution is parametrized with a scale parameter $\vartheta > 0$ and a shape parameter $k > 0$ and is given by [44]

$$g(x) = \frac{x^{k-1}\exp\left(-\frac{x}{\vartheta}\right)}{\vartheta^{k}\Gamma(k)}, \quad x > 0, \tag{1}$$

where $\Gamma(k)$ is the gamma function. The parameter k influences the shape of the distribution function and thus affects its symmetry and width. For a large shape parameter ($k \geqslant 12$) the gamma distribution resembles a Gaussian with narrow peak width. With decreasing k, the peak shape becomes increasingly asymmetric and broad. ϑ determines the dispersion of the distribution function, while the mean value is $\mu = k\vartheta$. The latter corresponds to the average domain size of our one-dimensional maze pattern. As a further refinement, we implement a hyperbolic-tangent domain-wall profile with a Bloch wall width according to the definition of Lilley [45,46] by convolving the +1 (–1) stepwise transitions with the corresponding kernel prior to performing the FFT [18]. We assume a domain-wall width of 40 nm, which is the average value calculated from the span of K_1 and K_2 determined from the structure factors (see below). The domain-wall width changes only slightly within the studied thickness range. The influence on the average domain sizes and the intensity profiles is in first approximation negligible. We took the average value of the domain-wall width for the sake of simplicity.

As an example, Fig. 5(b) gives the comparison of the intensity profile measured at $t_{\mathrm{Co,total}} = 54.6 \pm 0.4$ Å (black circles) and the simulated intensity profile (blue solid line) using a scale parameter $\vartheta = 18.3$ and a shape parameter $k = 4$. The simulated profiles are scaled in intensity to match the experimental profiles. The very same procedure brings the simulated and experimental profiles to a very good agreement up to t_{Critical}. From Fig. 5(b), an average one-dimensional domain size of $D_{\mathrm{gamma}} = k\vartheta = 73$ nm is obtained, whereas the domain size taken from the peak maximum gives $D_{Q_{\max}} = \pi/Q_{\max} = 83.5$ nm. The deviation of the two values amounts to 12.6%. Assuming a Gaussian size distribution, the peak position of the structure factor $Q_{\max}$ is commonly used to determine the average domain size $D_{Q_{\max}} = \pi/Q_{\max}$.

Hence our analysis points to a discrepancy between D_{gamma} and $D_{Q_{\max}}$. The generally used method apparently overestimates the average domain size of the real-space domain pattern in the case of the labyrinthlike domain pattern. In Fig. 5(a) $D_{Q_{\max}}$ is plotted versus D_{gamma} for the different Co thicknesses along the wedge. The plot reveals a linear relation

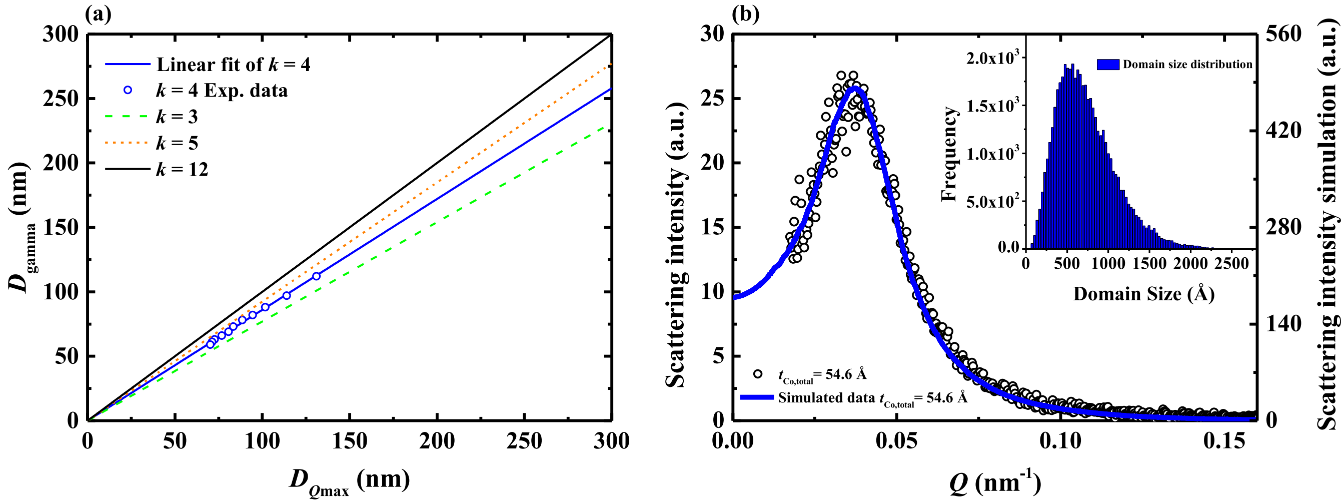

FIG. 5. (a) Relation between the domain size $D_{\mathrm{gamma}} = \vartheta k$ versus $D_{Q_{\max}} = \pi / Q_{\max}$. Values from the intensity profiles fitted to the experimental data are given by blue circles. The orange and green dashed lines show the dependences for two different k values and the black solid line illustrates the Gaussian distribution. (b) Intensity profile extracted from the diffraction pattern at $t_{\mathrm{Co,total}} = 54.6 \pm 0.4$ Å (open symbols) and the corresponding simulated intensity profile (blue solid line) obtained by a FFT of a one-dimensional domain pattern of gamma-distributed domain sizes. A histogram of this distribution is shown in the inset. A shape parameter of $k = 4$ and an average domain size of $D_{\mathrm{gamma}} = 73$ nm are used as input parameters.

between the two values. The black solid line corresponds to $D_{\mathrm{gamma}} = D_{Q_{\max}}$ taking a shape parameter $k \geqslant 12$. The blue symbols and line represent the experimental findings and best fit results for all structure factors below t_{Critical}. The orange and green dashed lines show the relation for $k = 3$ and $k = 5$.

A similar observation, i.e., a shift of the first-order peak position to lower $Q_{\max}$, has been found by Hellwig *et al.* [20] in the transition from spatially aligned to slightly disordered stripe domains. Miguel *et al.* [19] concluded that this implies that $Q_{\max}$ tends to overestimate the real average domain size in the disordered case. The authors suppose that the latter overestimation is the reason for the deviations in average domain size derived from magnetic force microscopy (MFM) and XRMS measurements.

With the model presented here, a perfect match of the measured and simulated intensity profiles [Fig. 3(c)] is obtained. Domain sizes of D_{gamma} ranging from 115 to 61 nm are found in the total Co thickness range of $t_{\mathrm{Co,total}} = 50.3 \pm 0.4$ Å to 58.5 ± 0.4 Å. Furthermore, the model demonstrates that the variation of peak widths [Fig. 3(c)] results solely from the change of ϑ at constant k and thus from a change in average domain size D_{gamma}. This implies that the maze pattern is scale invariant in the above-mentioned thickness range. The latter is evident from the measurements when normalizing the intensity profiles to the individual peak maxima and position ($Q_{\max}$). With the normalization all profiles fall on a universal curve [Fig. 6, inset].

We note that one striking observation shown in Fig. 3(c) has not been addressed so far. Beyond a total Co thickness of $t_{\mathrm{Critical}} = 58.5 \pm 0.4$ Å the structure factor remains constant in Q [Fig. 3(c)] which means, according to the model, that the domain size does not change anymore. The intensity, however, continues to drop for the remaining three structure factors ($t_{\mathrm{Co,total}} = 59.5 \pm 0.4$ Å to 61 ± 0.4 Å), which means that the intensity drop apparently has a different origin. One possible explanation is that the out-of-plane component of the magnetization is reduced. Such behavior can be expected within the spin-reorientation transition when magnetization canting is effective [21,30,31,47–49]. In addition, the fit via

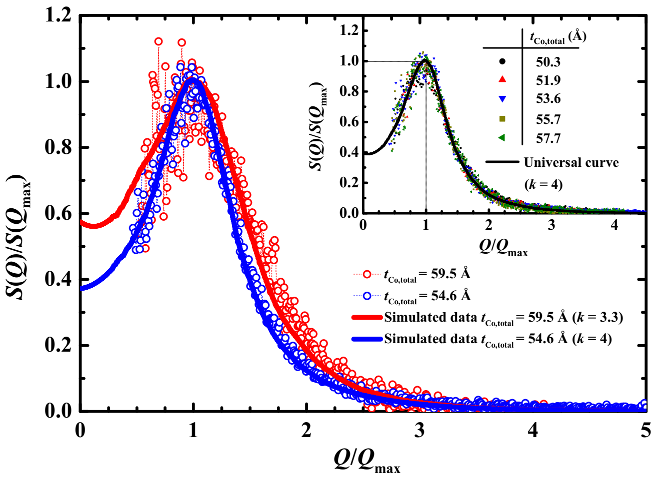

FIG. 6. Intensity profile at $t_{\mathrm{Co,total}} = 54.6$ Å normalized to the peak maximum and position $Q_{\max}$ (blue open symbols). For comparison a normalized intensity profile at $t_{\mathrm{Co,total}} = 59.5$ Å is plotted (red open symbols). The widths of both structure factors are different, indicating structural changes of the domain pattern at t_{Critical}. The simulated data indicate a change of the shape parameter of the gamma distribution from $k = 4$ to 3.3 (red and blue lines). The inset shows the normalized intensity profiles in the thickness range of $t_{\mathrm{Co,total}} = 50.3$ to 57.7 Å. Every second profile is plotted for the sake of better representation. The black curve displays the normalized simulated intensity profile with a shape parameter $k = 4$ which is denoted as a universal curve for all profiles.

the model reveals that the shape parameter has to be changed from $k = 4$ to 3.3 [Fig. 6] which means that the domain size distribution is varied above t_{Critical}. The profiles above t_{Critical}, however, are again best described by an identical shape parameter $k = 3.3$. Hence we have to assume that not only the magnetization canting sets in but the domain pattern also changes its characteristics.

VI. EXTRACTING THE MAGNETIC ANISOTROPY CONSTANTS

The directional free energy density of a magnetic thin film in second-order approximation F is given by [50,51]

$$F = K_{1,\mathrm{eff}}\sin^2\theta + K_2\sin^4\theta, \tag{2}$$

$$K_{1,\mathrm{eff}} = K_{1\mathrm{V}} + \frac{2K_{\mathrm{s}}}{t_{\mathrm{Co,single}}} - \frac{\mu_0}{2}M_{\mathrm{s}}^2, \tag{3}$$

where θ is the angle between the surface normal and the magnetization, $K_{1,\mathrm{eff}}$ is the effective first-order anisotropy constant, K_2 the second-order anisotropy constant, $K_{1\mathrm{V}}$ the volume anisotropy, K_{s} the surface and interface contribution of the anisotropy, $t_{\mathrm{Co,single}}$ the Co single-layer thickness. The last term in Eq. (3) represents the shape anisotropy with the saturation magnetization M_{s}. The increasing Co thickness causes the magnetostatic self-energy to increase, which prefers the in-plane orientation of magnetization. The thickness increase causes a decrease of $K_{1,\mathrm{eff}}$ and eventually a sign change in systems with strong perpendicular surface anisotropy. The magnetic film can reduce the magnetostatic self-energy when domains are created. The gain in dipolar energy is counterbalanced by excess of domain-wall energy. Due to the reduction of $K_{1,\mathrm{eff}}$, the domain-wall energy becomes smaller on thickness increase which allows for a more efficient reduction of dipolar energy via shrinking of the domains. As a proof of principle for the proposed structure-factor modulation we use the evolution of the domain sizes to determine the magnetic anisotropy of the Co/Pd multilayers.

In the second-order anisotropy approximation a phase diagram [48–50,52] (in the $K_{1,\mathrm{eff}}/K_2$ plane) is put forward. In the range $-2K_2 \leqslant K_{1,\mathrm{eff}} < 0$ magnetization canting takes place, separating the out-of-plane orientation for $K_{1,\mathrm{eff}} \geqslant 0$ and the in-plane orientation for $K_{1,\mathrm{eff}} < -2K_2$. At $K_{1,\mathrm{eff}} = 0$, the second-order anisotropy constant K_2 can be calculated from the equilibrium domain size utilizing the analytical expression given in Ref. [25]. If we assume that the system enters the canted phase at the thickness where the Q vector remains constant, i.e., $D_{\mathrm{gamma}} = 61$ nm and $t_{\mathrm{Critical}} = 58.5 \pm 0.4$ Å, the second-order anisotropy becomes $K_2 = 114.3 \pm 23.8\,\mathrm{kJ/m^3}$.

For $K_{1,\mathrm{eff}} > 0$, the domain-wall energy is a function of $K_{1,\mathrm{eff}}$ and K_2 [26]. The balance between overall cost of total domain-wall energy and reduction of stray-field energy determines the equilibrium domain size [53,54]. The latter theory is used to calculate $K_{1,\mathrm{eff}}$, assuming a constant $K_2 = 114.3 \pm 23.8\,\mathrm{kJ/m^3}$ in the small range of Co thicknesses. The first-order anisotropy constant varies from $K_{1,\mathrm{eff}} = 70.8 \pm 26.2\,\mathrm{kJ/m^3}$ to $2.8 \pm 14.6\,\mathrm{kJ/m^3}$ over a total Co thickness range from $t_{\mathrm{Co,total}} = 50.3 \pm 0.4$ Å to 57.7 ± 0.4 Å. Above t_{Critical}, we have assumed in first approximation that the decrease of the magnetic scattering amplitudes results from the reduction of the out-of-plane component of magnetization due to canting ($K_{1,\mathrm{eff}} < 0$). The signal is proportional to the square of the cosine of the canting angle θ_{c}, while the starting point of the canting (normal component of $M = M_{\mathrm{s}}$) is set at t_{Critical}. Utilizing the integrated intensities for the determination of the canting angle and using Eq. (4) [25] and $K_2 = 114.3 \pm 36.3\,\mathrm{kJ/m^3}$ the first-order anisotropy can be calculated.

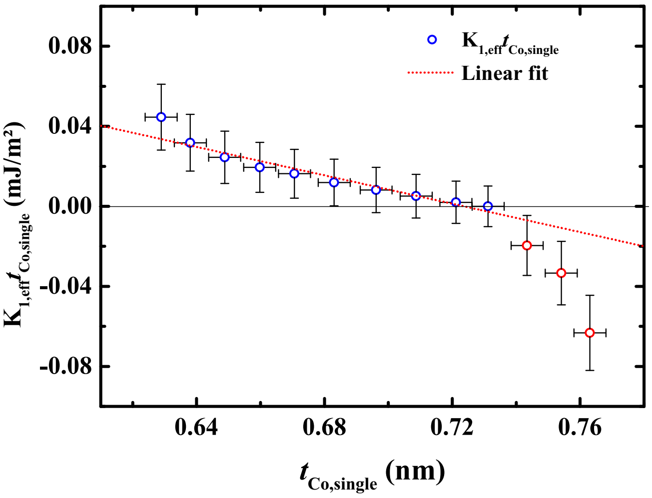

FIG. 7. $K_{1,\mathrm{eff}}t_{\mathrm{Co,single}}$ versus Co thickness of the Co/Pd multilayer. The values for $K_{1,\mathrm{eff}}t_{\mathrm{Co,single}} > 0$ (blue dots) are calculated using the analytical expression in Ref. [25] (see text), and a linear fit is shown. The values for $K_{1,\mathrm{eff}}t_{\mathrm{Co,single}} < 0$ are calculated using the integrated scattering intensities and the expression for the canting angle [Eq. (4)].

$$K_{1,\mathrm{eff}} = -2K_2\sin^2\theta_{\mathrm{c}}. \tag{4}$$

The results of the analysis for $K_{1,\mathrm{eff}}$ are plotted in Fig. 7. The dependence of $K_{1,\mathrm{eff}}\,t_{\mathrm{Co,single}}$ on thickness $t_{\mathrm{Co,single}}$ should give a straight line if the driving parameter is the thickness [Eq. (3)]. Obviously, the data below t_{Critical} fit a line quite well while the $K_{1,\mathrm{eff}}$ values in the canting regime deviate considerably from the former line. As the range of thicknesses investigated here is extremely small one can rule out substantial changes of the structure and a linear dependence is well suited. In the thickness range below t_{Critical} the slope of the plot is equal to the bulk anisotropy $K_{1\mathrm{V}} = 0.93 \pm 0.04\,\mathrm{MJ/m^3}$ while the intercept gives twice the interface anisotropy $K_{\mathrm{s}} = 0.14 \pm 0.02\,\mathrm{mJ/m^2}$. The values are in good agreement with measurements of single and multilayer films [37,55,56]. Hence it must be concluded that for $t < t_{\mathrm{Critical}}$ our model gives a very good agreement with what can be expected for the multilayers while for $t > t_{\mathrm{Critical}}$ the assumption for deducing the anisotropy has to be put into question.

In the preceding section it was mentioned that the structure factor changes at t_{Critical}, which has been assumed to be due to alterations of characteristics of the domain pattern. So far, it is not clear which property of the domain structure causes the change of the structure factor, e.g., change of microstructure and/or domain walls. It is, however, obvious that the scaling of the scattering intensity in the high-thickness range on the intensity at t_{Critical} is not correct.

VII. CONCLUSIONS

We performed x-ray resonant magnetic scattering experiments on a wedge-shaped Co/Pd multilayer sample to study a locally varying disordered magnetic maze domain structure. X-ray scattering intensity profiles extracted from magnetic diffraction patterns reveal variations of the peak position, width, and intensity. We propose a simple one-dimensional model to describe the observed radial distribution of the x-ray scattering intensity. A one-dimensional model using gamma-distributed domain sizes gives very good agreement with the experimental findings. In the range of perpendicular magnetization the structure factor of the maze pattern is best reproduced by a fixed shape parameter $k = 4$ which implies a scale invariance of the maze domain pattern in this range and hence an intrinsic symmetry, independent of the thickness or domain size variation. By introducing the additional shape parameter in our model, we are able to predict and compare intrinsic symmetry properties of magnetic domain patterns. Slight changes of symmetry, e.g., originating from external excitations, can be mapped out with our model.

Additionally we found a discrepancy of 12.6% comparing the average domain size calculated from the peak value of the structure factor and from fitting our model. Therefore, the commonly used method apparently overestimates the average domain size of the real-space domain pattern for the case of the disordered maze domain pattern.

For larger thicknesses $t > t_{\mathrm{Critical}}$ (supposed to be the transition to the canted phase) the shape parameter has to be changed from $k = 4$ to 3.3 to describe the scattering reasonably well. The different asymmetry parameter hints to modifications of magnetic microstructure. As a proof of principle we use the obtained information from the scattering experiment to determine thickness-dependent magnetic anisotropies of the Co/Pd multilayer wedge. The magnetic analysis proves the model to be correct in the range of perpendicular orientation of magnetization. The magnetic properties that come out of the analysis are in good agreement with published results.

Due to the high sensitivity and lateral resolution of the XRMS technique small variations of domain size can be resolved. Thus our model allows for the determination of magnetic anisotropies in a thickness range of only a few angstroms.

ACKNOWLEDGMENTS

We acknowledge funding by DFG within SFB 668, as well as by BMBF via FSP 301/05K10GU4. R.A. and C.W. gratefully acknowledge support from DFG Project No. SCHN353/17-1. L.M. and S.S. acknowledge support from DFG within SFB 925. This work has been supported by the excellence cluster "The Hamburg Centre for Ultrafast Imaging—Structure, Dynamics, and Control of Matter on the Atomic Scale" of the Deutsche Forschungsgemeinschaft. M.H.B. acknowledges the Knut and Alice Wallenberg Foundation for its financial support. We thank Dr. Juliane Thielsch and Dr. Thomas G. Woodcock for providing the data of the domain size distribution of a Nd-Fe-B sample. We thank the P04 staff for the support and technical assistance. We thank Nikolai Mikuszeit for bringing the gamma distribution to our attention.

---

[1] P. Fischer, G. Schütz, G. Schmahl, P. Guttmann, and D. Raasch, Z. Phys. B: Condens. Matter **101**, 313 (1996).

[2] W. Chao, B. D. Harteneck, J. A. Liddle, E. H. Anderson, and D. Attwood, Nature **435**, 1210 (2005).

[3] P. Fischer, IEEE Trans. Magn. **51**, 0800131 (2015).

[4] S. Eisebitt, J. Lüning, W. F. Schlotter, M. Lörgen, O. Hellwig, W. Eberhardt, and J. Stöhr, Nature **432**, 885 (2004).

[5] S. Schaffert, B. Pfau, J. Geilhufe, C. M. Günther, M. Schneider, C. von Korff Schmising, and S. Eisebitt, New J. Phys. **15**, 093042 (2013).

[6] S. Streit-Nierobisch, D. Stickler, C. Gutt, L.-M. Stadler, H. Stillrich, C. Menk, R. Frömter, C. Tieg, O. Leupold, H. P. Oepen, and G. Grübel, J. Appl. Phys. **106**, 083909 (2009).

[7] D. Stickler, R. Frömter, H. Stillrich, C. Menk, C. Tieg, S. Streit-Nierobisch, M. Sprung, C. Gutt, L.-M. Stadler, O. Leupold, G. Grübel, and H. P. Oepen, Appl. Phys. Lett. **96**, 042501 (2010).

[8] A. Tripathi, I. McNulty, and O. G. Shpyrko, Opt. Express **22**, 1452 (2014).

[9] X. Shi, P. Fischer, V. Neu, D. Elefant, J. C. T. Lee, D. A. Shapiro, M. Farmand, T. Tyliszczak, H.-W. Shiu, S. Marchesnini, S. Roy, and S. D. Kevan, Appl. Phys. Lett. **108**, 094103 (2016).

[10] J. B. Kortright, S.-K. Kim, G. P. Denbeaux, G. Zeltzer, K. Takano, and E. E. Fullerton, Phys. Rev. B **64**, 092401 (2001).

[11] M. Blume, J. Appl. Phys. **57**, 3615 (1985).

[12] K. Chesnel, M. Belakhovsky, S. Landis, J. C. Toussaint, S. P. Collins, G. van der Laan, E. Dudzik, and S. S. Dhesi, Phys. Rev. B **66**, 024435 (2002).

[13] J. P. Hannon, G. T. Trammell, M. Blume, and D. Gibbs, Phys. Rev. Lett. **61**, 1245 (1988).

[14] E. E. Fullerton, O. Hellwig, K. Takano, and J. B. Kortright, Nucl. Instrum. Methods Phys. Res., Sect. B **200**, 202 (2003).

[15] H. A. Dürr, E. Dudzik, S. S. Dhesi, J. B. Goedkoop, G. van der Laan, M. Belakhovsky, C. Mocuta, A. Marty, and Y. Samson, Science **284**, 2166 (1999).

[16] B. Vodungbo, B. Tudu, J. Perron, R. Delaunay, L. Müller, M. H. Berntsen, G. Grübel, G. Malinowski, C. Weier, J. Gautier, G. Lambert, P. Zeitoun, C. Gutt, E. Jal, A. H. Reid, P. W. Granitzka, N. Jaouen, G. L. Dakovski, S. Moeller, M. P. Minitti *et al.*, Sci. Rep. **6**, 18970 (2016).

[17] C. Gutt, S. Streit-Nierobisch, L. M. Stadler, B. Pfau, C. M. Günther, R. Könnecke, R. Frömter, A. Kobs, D. Stickler, H. P. Oepen, R. R. Fäustlin, R. Treusch, J. Feldhaus, E. Weckert, I. A. Vartanyants, M. Grunze, A. Rosenhahn, T. Wilhein, S. Eisebitt, and G. Grübel, Phys. Rev. B **81**, 100401(R) (2010).

[18] B. Pfau, S. Schaffert, L. Müller, C. Gutt, A. Al-Shemmary, F. Büttner, R. Delaunay, S. Flewett, R. Frömter, J. Geilhufe, E. Guehrs, C. M. Günther, R. Hawaldar, M. Hille, N. Jaouen, A. Kobs, K. Li, J. Mohanty, H. Redlin, W. F. Schlotter *et al.*, Nat. Commun. **3**, 1100 (2012).

[19] J. Miguel, J. F. Peters, O. M. Toulemonde, S. S. Dhesi, N. B. Brookes, and J. B. Goedkoop, Phys. Rev. B **74**, 094437 (2006).

[20] O. Hellwig, G. P. Denbeaux, J. B. Kortright, and E. E. Fullerton, Physica B **336**, 136 (2003).

[21] Y. T. Millev, H. P. Oepen, and J. Kirschner, Phys. Rev. B **57**, 5837 (1998).

[22] Y. T. Millev, H. P. Oepen, and J. Kirschner, Phys. Rev. B **57**, 5848 (1998).

[23] P. C. D. Hobbs, D. W. Abraham, and H. K. Wickramasinghe, Appl. Phys. Lett. **55**, 2357 (1989).

[24] J. Li, N. Chen, D. Wei, and M. Futamoto, IEEE Trans. Magn. **51**, 2001005 (2015).

[25] D. Stickler, R. Frömter, H. Stillrich, C. Menk, H. P. Oepen, C. Gutt, S. Streit-Nierobisch, Lorenz-M. Stadler, G. Grübel, C. Tieg, and F. Yakhou-Harris, Phys. Rev. B **84**, 104412 (2011).

[26] W. Sucksmith and F. E. Thomson, Proc. R. Soc. A **225**, 362 (1954).

[27] A. Maziewski, V. Zablotskii, and M. Kisielewski, Phys. Status Solidi A **189**, 1001 (2002).

[28] M. Speckmann, H. P. Oepen, and H. Ibach, Phys. Rev. Lett. **75**, 2035 (1995).

[29] M. Wellhöfer, M. Weissenborn, R. Anton, S. Pütter, and H. P. Oepen, J. Magn. Magn. Mater. **292**, 345 (2005).

[30] H. Stillrich, C. Menk, R. Frömter, and H. P. Oepen, J. Appl. Phys. **105**, 07C308 (2009).

[31] H. Stillrich, C. Menk, R. Frömter, and H. P. Oepen, J. Magn. Magn. Mater. **322**, 1353 (2010).

[32] J. Viefhaus, F. Scholz, S. Deinert, L. Glaser, M. Ilchen, J. Seltmann, P. Walter, F. Siewert, Nucl. Instrum. Methods Phys. Res., Sect. A **710**, 151 (2013).

[33] K. Bagschik, R. Frömter, L. Müller, W. Roseker, J. Bach, P. Staeck, C. Thönnißen, S. Schleitzer, M. H. Berntsen, C. Weier, R. Adam, J. Viefhaus, C. M. Schneider, G. Grübel, and H. P. Oepen, Opt. Express **24**, 23162 (2016).

[34] N. Nakajima, T. Koide, T. Shidara, H. Miyauchi, H. Fukutani, A. Fujimori, K. Iio, T. Katayama, M. Nyvlt, and Y. Suzuki, Phys. Rev. Lett. **81**, 5229 (1998).

[35] R. Bodenberger and A. Hubert, Phys. Status Solidi A **44**, K7 (1977).

[36] E. E. Underwood, *Quantitative Stereology* (Addison-Wesley, Reading, MA, 1970).

[37] G. Winkler, A. Kobs, A. Chuvilin, D. Lott, A. Schreyer, and H. P. Oepen, J. Appl. Phys. **117**, 105306 (2015).

[38] A. Kobs, Magnetogalvanic effects in ferromagnets of reduced dimensions, Ph.D. thesis, University of Hamburg, 2013.

[39] G. Schütz, W. Wagner, W. Wilhelm, P. Kienle, R. Zeller, R. Frahm, and G. Materlik, Phys. Rev. Lett. **58**, 737 (1987).

[40] C. T. Chen, F. Sette, Y. Ma, and S. Modesti, Phys. Rev. B **42**, 7262 (1990).

[41] J. Stöhr, H. A. Padmore, S. Anders, T. Stammler, and M. R. Scheinfein, Surf. Rev. Lett. **5**, 1297 (1998).

[42] W. Burger and M. J. Burge, *Digital Image Processing* (Springer-Verlag, Berlin, 2008).

[43] J. Thielsch, H. Stopfel, U. Wolff, V. Neu, T. G. Woodcock, K. Güth, L. Schultz, and O. Gutfleisch, J. Appl. Phys. **111**, 103901 (2012).

[44] C. Forbes, M. Evans, N. Hastings, and B. Peacock, *Statistical Distributions*, 4th ed. (J. Wiley & Sons, Hoboken, NJ, 2011).

[45] B. A. Lilley, Philos. Mag. **41**, 792 (1950).

[46] A. Hubert and R. Schäfer, *Magnetic Domains: The Analysis of Magnetic Microstructure* (Springer-Verlag, Berlin, Heidelberg, 2009).

[47] R. Frömter, H. Stillrich, C. Menk, and H. P. Oepen, Phys. Rev. Lett. **100**, 207202 (2008).

[48] Y. Millev and J. Kirschner, Phys. Rev. B **54**, 4137 (1996).

[49] M. BingFeng, Y. T. Millev, L. Sun, B. You, W. Zhang, and H. Ding, Sci. China: Phys., Mech. Astron. **56**, 70 (2013).

[50] F. J. A. den Broeder, W. Hoving, and P. J. H. Bloemen, J. Magn. Magn. Mater. **93**, 562 (1991).

[51] M. B. Stearns, in *Landolt-Börnstein: Magnetic Properties of Metals: 3d, 4d and 5d Elements, Alloys and Compounds III*, Vol. 19, Pt. a, edited by H. P. J. Wijn (Springer, Verlag, Berlin, 1986).

[52] H. Casimir, J. Smit, U. Enz, J. F Fast, H. P. J. Wijn, E. W. Gorter, A. J. W. Duyvesteyn, J. D. Fast, and J. J. De Jong, J. Phys. Radium **20**, 360 (1959).

[53] B. Kaplan and G. Gehring, J. Magn. Magn. Mater. **128**, 111 (1993).

[54] Y. Millev, J. Phys.: Condens. Matter **8**, 3671 (1996).

[55] P. F. Carcia, A. D. Meinhaldt, and A. Suna, Appl. Phys. Lett. **47**, 178 (1985).

[56] H. J. G. Draaisma, W. J. M. de Jonge, and F. J. A. den Broeder, J. Magn. Magn. Mater. **66**, 351 (1987).